纳米压痕法测量 80Au/20Sn 焊料热力性能

张国尚[1]， 荆洪阳[1]， 徐连勇[1]， 魏 军[2]， 韩永典[1]
（1. 天津大学 材料科学与工程学院，天津 300072；
2. 新加坡制造技术研究院，新加坡 638075）

张国尚

摘 要：采用恒加载速率/载荷纳米压痕试验测量了 25，75，125 及 200 ℃下 80Au/20Sn 焊料的热力性能. 结果表明，加载速率、施加载荷和温度对压痕载荷—位移曲线影响显著；80Au/20Sn 焊料具有较强的加载速率敏感性，显著的尺寸效应，125 和 200 ℃下出现了明显的“挤出”现象；应用半椭圆模型对产生“挤出”的接触面积修正后基于 Oliver-Pharr 方法求得了弹性模量和硬度；弹性模量和硬度随加载速率的增加迅速增大后趋于稳定，随施加载荷增加先减小后几乎保持不变，随温度升高而急聚降低.

关键词：80Au/20Sn 焊料；纳米压痕；热力性能
中图分类号：TB302.3 文献标识码：A 文章编号：0253－360X(2009)09－0053－04

0 序 言

长期以来，锡铅焊料被广泛应用于电子封装中. 近年来，由于日益增加环保要求以及现代大功率电子和光电子器件对焊点可靠性要求的提高，迫切需要具有良好抗蠕变和热疲劳行为的焊料. 在已开发成功的无铅焊料中，80Au/20Sn 钎料因具有良好的高温性能、优越的耐腐蚀性能、良好的导电导热性、较高的力学性能并且能在无助焊剂条件下进行焊接等特性，被作为密封和芯片焊接材料广泛应用于对可靠性要求极高的大功率电子器件及光电子器件互连中[1]. 在上述应用中，有关 80Au/20Sn 焊料的制造工艺已被广泛研究，主要集中在连接质量、冶金交互作用以及 Au-Sn 焊料凸点的形成上. 除可制造性和可焊接性，还需要对焊料的热力性能有深入理解，以便进行可靠性设计及与其它焊料进行比较，然而这方面的研究目前却少有报道，因此深入研究其热力性能非常必要.

焊料的热力性能通常采用标准拉伸测试和传统单轴拉伸蠕变试验等测试方法，这些方法对于 80Au/20Sn 焊料及其它许多无铅焊料需耗费大量的人力、物力及时间，有必要寻找一种简单易行的替代方法. 纳米压痕法作为一种便捷、非破坏性及低成本的测试方法，通过测量压入载荷与压入深度的连续变化，可以获得材料的弹性模量、蠕变硬度、屈服应力、蠕变等力学性能以及很多应用场合下传统力学方法无法获得的金属表面改性层、厚薄膜电路、焊接接头界面等信息. 目前纳米压痕试验方法主要有恒载荷法、恒加载速率法、施加恒加载速率/载荷法. 由于钎料热力性能的应变速率相关性，文中采用恒加载速率/载荷法，分析加载速率、载荷及温度对 80Au/20Sn 焊料热力性能的影响，获取不同温度下的弹性模量和蠕变硬度.

收稿日期：2008－11－14
基金项目：教育部新世纪优秀人才基金资助项目(NCET－06－0235)；国家自然科学基金资助项目(50575160)；教育部高等学校博士点基金资助项目(20050056035)

1 试验方法

1.1 测试原理

图 1 为纳米压痕测试得到的典型载荷—位移(F-h)曲线. 试验时先以恒定加载速率压入试样表面，在载荷不断增加的过程中压入深度呈同步非线性增加. 当载荷达到预先设定的最大值 F_m 后保持一段时间，对于具备蠕变特征的材料而言，尽管此时载荷不再增加，但仍可观察到蠕变位移. 当达到预先设定的保持时间后，载荷开始以一定的速率卸载直至减小为零，而此时的残余压入深度 h_f 表明材料经受了不可回复的塑性变形.

Oliver-Pharr 法是普遍接受的确定弹性模量的一种方法，该方法假设卸载曲线的初始阶段为线性，通过定义弹性接触刚度 S(图1)为卸载初始阶段卸载

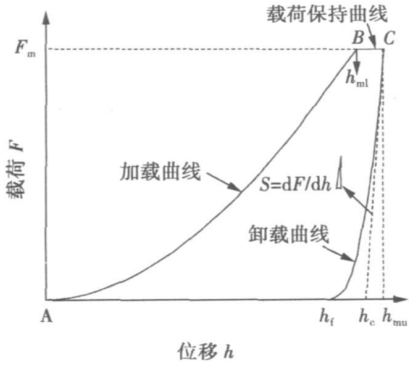

图 1 钎料合金的典型 F-h 曲线

Fig. 1 Typical indentation load-displacement curve for solder alloy

曲线的斜率,给出了弹性模量的计算[2,3].

首先确定试样材料的约化模量 E_r,即

$$E_r=\frac{\sqrt{\pi}}{2\beta}\frac{S}{\sqrt{A}} \tag{1}$$

式中:S 为卸载曲线初始阶段的斜率;β 为取决于压子几何形状的常数,对于三角锥截面的 Berkovich 压子,β=1.034;A 为正向接触投影面积.利用几何关系,可以得到理想的三角锥压子垂直表面的压痕投影面积为

$$A=24.5h_c^2 \tag{2}$$

式中:h_c 为接触压深,定义为压子与试件的真实接触深度.接触压深与最大压痕深度 h_{mu} 的关系为

$$h_c=h_{mu}-\varepsilon\frac{F_m}{S} \tag{3}$$

式中:ε 为与压子几何形状有关的常数,对 Berkovich 压子,取经验值 ε=0.72.

试样材料的弹性模量 E 由下式确定,即

$$\frac{1}{E_r}=\frac{1-\upsilon_i^2}{E_i}+\frac{1-\upsilon^2}{E} \tag{4}$$

式中:E_i,υ_i 分别为压子材料的弹性模量和泊松比;υ 为试样材料的泊松比.

按照通常的材料硬度的定义方法,压痕法得到的硬度取最大载荷下的平均压力为[2]

$$p=\frac{F_m}{A} \tag{5}$$

1.2 测试材料

所用材料为共晶 80Au/20Sn 焊料合金,熔点为 279.4 ℃±0.1 ℃.为了得到与实际封装中焊点相似的微观组织,焊料棒浇铸时采用空冷的方法.随后对得到的高纯度铸态焊料棒进行机械切削,加工成截面为 0.4 mm×1.55 mm 的带状试样.每一试样先用 2000 号的 SiC 砂纸仔细研磨,再依次用 3,1,0.5 μm的 K 形铝悬浮液抛光,最后用 0.05 μm 的硅溶胶抛光液抛光.抛光完成后,所有试样在 60 ℃、氮气环境下进行 24 h 退火消除残余应力.

1.3 测试设备

采用配备高温环境箱的 MTS XP 型纳米压痕仪进行测试,该设备位移分辨率为 0.01 nm,载荷分辨率为 50 nN,控温精度 ±0.1 ℃,压子采用 Berkovich 金刚石压子.测试前先在熔融的石英(SiO_2)支架上校正压痕系统,并确定该设备负载结构的柔性和压子面积函数.

1.4 测试步骤

首先,考虑加载速率对热力性能的影响.恒定的加载速率分别为 0.2,0.5,1,10,40 及 80 mN/s.为了获得整体的力学响应,采用 400 mN 的大载荷.测试过程中,温度控制在 25 ℃±0.1 ℃,将 Berkovich 压子以 10 mN/s 的速度接触样品的表面,测试分成 3 个阶段:以恒定的加载速率压入样品,直到达到预定最大载荷 F_m;在最大载荷 F_m 下保持 300 s 以进行蠕变,卸载,卸载速率为 10 mN/s.其次,分析施加载荷对热力性能的影响.加/卸载速率为10 mN/s,最大载荷分别为 100,200,300 和 500 mN.最后,研究温度对热力性能的影响.在加/卸载速率为 10 mN/s,最大载荷为 400 mN,测试温度分别为 75,125 及 200 ℃时进行压痕测试.

以上所有测试中,相邻压痕及相邻压痕线之间的距离都设置为 350 μm,以避免产生任何残余应力及邻近压痕之间可能出现的"挤出"或"沉陷"现象.每一测试条件下对试样进行三次测量,然后取平均值,测试完成后用 JOEL JSM-6360A SEM 对压痕进行微观组织分析.

2 试验结果及讨论

2.1 加载速率对 80Au/20Sn 焊料热力性能的影响

图 2 为不同加载速率压痕试样的载荷—位移曲线,可以看出 80Au/20Sn 焊料的变形与加载速率有关,较低加载速率产生了较大的位移变化.在加载阶段,较低的加载速率导致了较大的压痕深度,即较低的压痕硬度和屈服应力,这是因为试样有足够的时间发生动态回复.在载荷保持阶段,压痕深度的变化表明在该阶段发生了蠕变.若将最大载荷压痕深度的变化量定义为蠕变位移,则较高的加载速率导致较大的蠕变位移,即导致了较高的蠕变应变率.

图 3 为加载速率对 80Au/20Sn 焊料的力学性能的影响,低加载速率的蠕变变形导致材料强度降低.弹性模量和蠕变硬度随着加载速率的增加而增

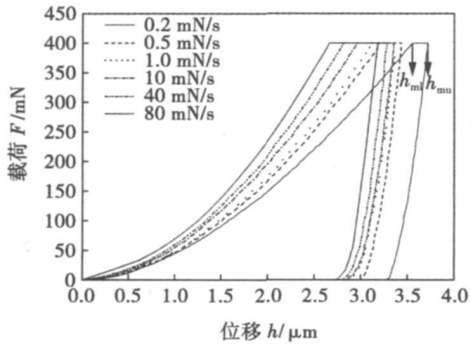

图 2　加载速率对载荷—位移曲线的影响

Fig. 2　Influence of loading rate on load-displacement curves

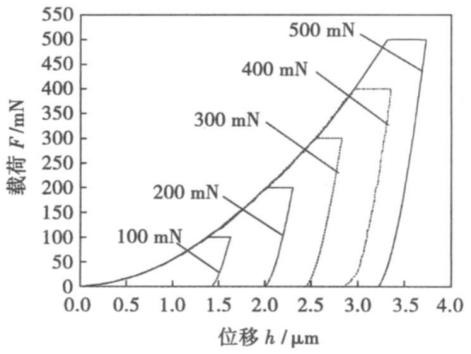

图 4　施加载荷对载荷—位移曲线的影响

Fig. 4　Influence of applied load on load-displacement curves

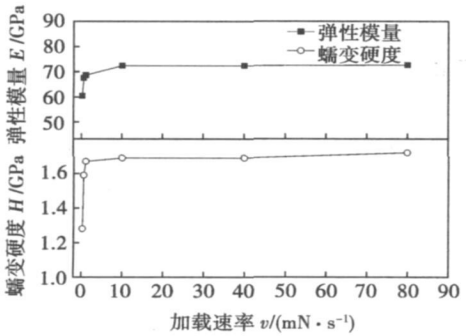

图 3　加载速率对力学性能的影响

Fig. 3　Variation of mechanical properities with loading rate

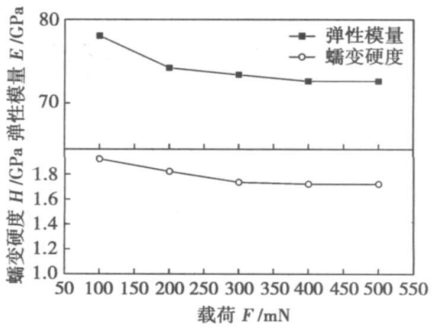

图 5　施加载荷对力学性能的影响

Fig. 5　Variation of mechanical properties with applied load

加，当加载速率增加到 5 mN/s 以上时，弹性模量和蠕变硬度几乎保持不变. 当测量中读数恒定时，即可获得材料的弹性模量和蠕变硬度. 由于这些力学性能参量通过卸载曲线获得，因此考虑压痕蠕变将会改进测量精度[4]. 该测试中由于卸载曲线没有出现明显的凸肚现象，所以可不进行校正.

2.2　施加载荷对 80Au/20Sn 焊料热力性能的影响

常温下 80Au/20Sn 焊料在不同施加载荷下的载荷—位移关系如图 4 所示. 从图中可以看出，压痕深度及蠕变位移随施加载荷增加而增加，但后者增幅较小. 施加载荷对力学性能的影响如图 5 所示，随着施加载荷的增加，弹性模量和硬度不断减小，直到数值达到恒定的平台，即 80Au/20Sn 焊料与许多材料一样表现出明显的尺寸效应.

2.3　温度对 80Au/20Sn 焊料热力性能的影响

图 6 为 80Au/20Sn 焊料在不同温度下的载荷—位移曲线. 显然，随着温度的增加，载荷—位移曲线朝着更大压痕深度的方向移动，蠕变位移随温度的增加而增加，并在 200 ℃时达到了最大值. 这是由于较高的温度下回复速率较快，加工硬化对蠕变的影响被显著减弱，因此焊料中蠕变速率增大，最终产生更大的蠕变位移.

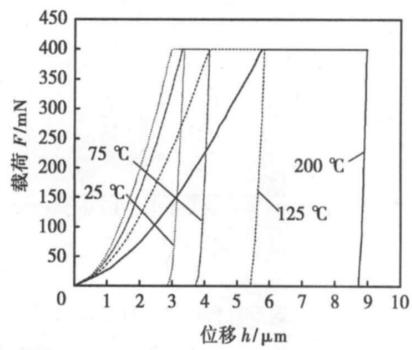

图 6　不同温度下的载荷—位移曲线

Fig. 6　Load versus displacement at various temperatures

图 7 为测试温度为 125 ℃时典型压痕 SEM 形貌，图中亮色区和暗色区分别为 Au_5Sn（ζ′）和 AuSn（δ）相，这表明施加的载荷足够大取得了整体力学响应. 在 125 和 200 ℃下，试样在压痕边缘出现了材料的“挤出”现象，温度越高“挤出”现象越明显，这表明发生了显著的塑性改变. 由于“挤出”现象会导

致低估真实接触面积，因此考虑“挤出”可以提高弹性模量和硬度的求解精度[3]．采用半椭圆模型[5]对出现“挤出”现象的结果进行了修正，不同温度对80Au/20Sn 焊料的力学性能如图 8 所示．从图 8 中可以看出，弹性模量和硬度随温度升高显著降低，加热过程中的软化及高温下的蠕变变形是 80Au/20Sn 焊料力学性能下降的主要原因．

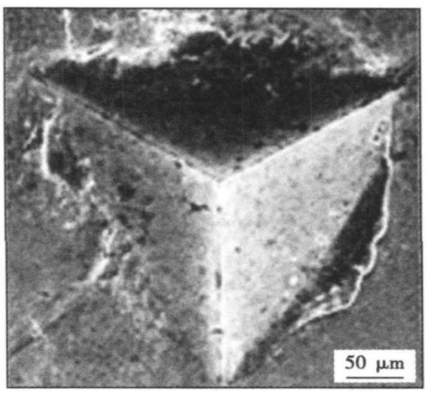

图 7 125 ℃下压痕的典型背散射电子形貌

Fig. 7 Typical backscattered electron image of indentation at 125 ℃

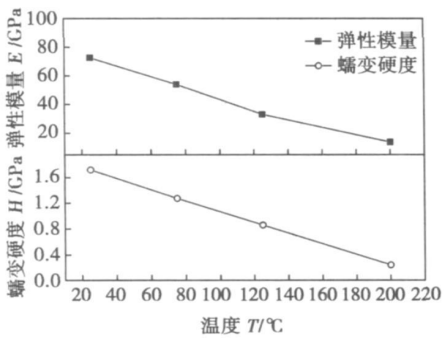

图 8 温度对力学性能的影响

Fig. 8 Variation of mechanical properities with temperature

3 结 论

（1）加载速率越大蠕变位移越大，而压痕深度越小；弹性模量和硬度随加载速率的增加而增加，但当加载速率增加到 5 mN/s 以上时基本保持不变．

（2）随着施加载荷的增加，压痕深度显著增加，而蠕变位移增加幅度较小；80Au/20Sn 焊料表现出明显的尺寸效应，即施加载荷增加时，弹性模量和硬度值减小，直到达到稳定的硬度平台．

（3）随着温度的升高，压痕深度和蠕变位移显著增加，弹性模量和硬度急骤降低；当温度高于 125 ℃时，压痕边缘出现了明显的“挤出”现象．

参考文献：

[1] Teo J W R, Ng F L, Goi L S K, *et al*. Microstructure of eutectic 80Au/20Sn solder joint in laser diode package[J]. Microelectronic Engineering, 2008, 85(3): 512－517.

[2] Oliver W C, Pharr G M. An improved technique for determining hardness and elastic modulus using load and displacement sensing indentation experiment[J]. Journal of Materials Research, 1992, 7(6): 1564－1583.

[3] Bolshakov A, Pharr G M. Influences of pileup on the measurement of mechanical properties by load and depth sensing indentation techniques[J]. Journal of Materials Research, 1998, 13(4): 1049－1058.

[4] Chudoba T, Richter F. Investigation of creep behavior under load during indentation experiments and its influence on hardness and modulus results[J]. Surface & Coatings Technology, 2001, 148(2－3): 191－198.

[5] Kese K, Li Z C. Semi-ellipse method for accounting for the pile-up contact area during nanoindentation with the berkovich indenter[J]. Scripta Materialia, 2006, 55(8): 699－702.

作者简介：张国尚，男，1977 年出生，博士研究生，工程师．主要从事电子产品封装设计及其可靠性研究工作．发表论文 6 篇．

Email：gshangz@126.com

tube 2.

Key words: explosive welding; three layer tube; numerical simulation; stand-off distance; strain-stress

Precision rapid prototyping of steel parts using TIG depositision technology LI Yulong, ZHANG Hua, ZHANG Guangyun, XU Jianning (Key Lab of Robot & Welding Automation, School of Mechanical & Electrical Engineering, Nanchang University, Nanchang 330031, China). p 37—40

Abstract: A rapid prototyping (RP) system is presented in this paper. This RP system is based on the tungsten inert gas (TIG) welding deposition technology, which includes a welding electrical source, a TIG welding torch, a wire feeder, a numerical controlled milling equipment, an industrial computer, an AD sampling card and etc. The TIG welding torch and wire feeder were used for weld deposition; the numerical controlled milling equipment was used for controlling the movement of the TIG torch and milling the deposited parts; the industrial computer was used for sampling data and feedbacking control during the deposition process. For resolving the problem of edge sink in weld deposited part, a fuzz control system based on voltage feedback was designed. A wall-shape part was deposited with the help of this fuzz control system. Then a cylinder-shape part with precise geometry size was deposited and milled in the RP system.

Key words: welding deposition; rapid prototyping (RP); voltage feedback control; milling with numerical control

Effect of inoculants Ti and Zr on microstructure and mechanical properties of 2219 Al-Cu alloy welding YANG Chenggang[1], GUO Xuming[2], XING Li[1] (1. School of Materials Science and Engineering, Nanchang University of Aeronautics, Nanchang 330063, China; 2. School of Materials Science and Engineering, Shenyang Institute of Aeronautical Engineering, Shenyang 110034, China). p 41—44

Abstract: Metal inert gas (MIG) welding was used to weld 2219 Al-Cu alloy with five kinds of filler metal, effect of the inoculants Ti and Zr additions in filler wires on the microstructures and properties of weld metal was investigated. The results showed that Ti and Zr was compatible, grain structures of weld were coarse columnar grains with a little Ti or Zr in filler wires, Al_3Ti and Al_3Zr were formed in the welding pool with additions of a little Ti and Zr in filler wires, which provided the heterogeneous nucleation sites for α(Al). The grain of the microstructure of weld metal was finer with the increasing of Ti and Zr compositions in filler wires. Intermetallic aluminized dispersoids $Al_3(Ti, Zr)$ were formed in weld metal with additions of large amounts of Ti and Zr in filler wires, which accelerated the heterogeneous nucleation of α(Al) and resulted in refining grains of the weld metal, so the tensile strength and elongation of weld joint were increased.

Key words: inoculants; 2219 Al-Cu alloy; heterogeneous nucleation; equiaxed grain

Microstructure and properties of Sn-Zn-Bi-(P, Nd) lead-free solders ZHOU Jian[1], FU Xiaoqing[1], SUN Yangshan[1], DING Kejian[2] (1. Jiangsu Key Laboratory of Advanced Metallic Materials, Southeast University, Nanjing 211189, China; 2. Jingerli Metal Company, Changzhou 213144, Jiangsu, China). p 45—48

Abstract: Microstructure, mechanical properties, oxidation resistance and wettability of Sn-8Zn-3Bi lead-free solder doping with P and Nd were studied in this paper. Primary Zn phase was observed in the microstructure of Sn-8Zn-3Bi alloying with separate P element. By adding P together with Nd not only the formation of the primary Zn phase can be inhibited, the massive microstructure of the solder also can be refined. It was the reason that the solder plastic improved, and the elongation reached 48%. P element in solder melts was apt to loss in the process of long term heating. A diffusion barrier layer could form at the surface of the Sn-8Zn-3Bi solder by doping with P and Nd, which reduced the loss of P, and the oxidation rate decreased as well. With the improved oxidation resistance, the Sn-8Zn-3Bi-0.1P-0.05Nd solder showed high wetting performance.

Key words: lead-free solder; Sn-Zn alloys; oxidation; mechanical properties

Ripple line fillet seams tracking control of a mobile robot for container welding GAO Yanfeng[1,2], XIAO Jianhua[1], ZHANG Hua[2] (1. School of Aviation & Mechanical Engineering, Nanchang Hangkong University, Nanchang 330031, China; 2. Robot Research Institute, Nanchang University, Nanchang 330031, China). p 49—52

Abstract: For the container ripple line fillet seams tracking, it is necessary not only to control welding-torch moving along with the seams, but also to adjust inclination of the the torch perpendicular to the welding surface. In this paper, a wheeled mobile welding robot with a cross-slider manipulator that can extend and turn was developed. A rotational arc sensor was used to detect the welding-torch deviations and inclinations simultaneously. Through controlling three joints coordinate movement, welding seam tracking and welding-torch inclination adjusting were achieved. The kinematics model of the mobile robot is established, and with fuzzy control theory, a controller was designed. Through actual welding experiments, the validity of the proposed method is proved.

Key words: mobile robot; welding seam tracking; welding-torch attitude control; rotational arc sensor

Thermomechanical characterization of 80Au/20Sn solder using nanoindentation ZHANG Guoshang[1], JING Hongyang[1], XU Lianyong[1], WEI Jun[2] (1. School of Material Science and Engineering, Tianjin University, Tianjin 300072, China; 2. Singapore Institute of Manufacturing Technology, 71 Nanyang Drive, Singapore 638075, Singapore). p 53—56

Abstract: The thermomechanical behaviors of the 80Au/20Sn solder at 25, 75, 125 and 200 ℃ were investigated by constant

loading rate/load nanoindentation tests. The results showed that the load-displacement curves depended on the loading rate, applied load and temperature strongly. The loading rate sensitivity, obvious size effect, piling up at 125 and 200 ℃ were observed. The elastic modulus and hardness were obtained using the Oliver-Pharr method after the contact area was modified based on the semi-ellipse method. The elastic modulus and hardness increase rapidly with the improved loading rate then reach an approximately steady stage, decrease initially as the increased load ultimately attain a steady-state value, decline greatly with the higher temperature.

Key words: 80Au/20Sn solder; nanoindentation; thermomechanical properties

Residual stress analysis of repair welding at different zone of Q345R welded joint based on finite element simulation SHEN Limin, GONG Jianming, YU Zhenggang, TU Shandong (College of Mechanical and Power Engineering, Nanjing University of Technology, Nanjing 210009, China). p 57—60, 64

Abstract: Because of its excellent properties, Q345R alloy is extensively used in the manufacture of pressure vessels and pipes. However, cracks often generate in a weldment made of this alloy for welding residual stress. Using finite element analysis software ABAQUS, a sequentially coupled welding thermal-stress procedure was developed to calculate the repair welding residual stress for different zones of Q345R welded joint. 3D repairing welding residual stress field was obtained and analyzed. The result shows that residual stress caused by repair welding increases than before, and longitudinal stress and transversal stress do not increase uniformly. The analysis from simulation results provides theoretical references for optimizing the repair welding parameters and controlling the repair welding stress.

Key words: Q345R; welding residual stress; repair welding; numerical simulation; finite element ABAQUS

Study on diffusion bonding TC4 to ZQSn10-2-3 using a Ni interlayer ZHAO He, CAO Jian, FENG Jicai (State Key Laboratory of Advanced Welding Production Technology, Harbin Institute of Technology, Harbin 150001, China). p 61—64

Abstract: Diffusion bonded joints were prepared between TC4 and ZQSn10-2-3 with nickel as an interlayer in vacuum. The microstructure of transition joints was investigated by scanning electron microscope and energy dispersive spectrometry. The typical interface of TC4/Ni/ZQSn 10-2-3 joint is TC4/β-Ti/Ti_2Ni/TiNi/$TiNi_3$/Ni/Cu(Cu, Ni)/ZQSn10-2-3. The optimum parameters were obtained in the condition of 830 ℃ for 30 min under 10 MPa by optimum experiments. The maximum shear strength was 130 MPa. The results showed the fracture was crystal morphology with a little plastic, and occurred proximity to $TiNi_3$ intermetallic layer in TC4/Ni side through X-ray diffraction analysis.

Key words: titanium alloy; tin-bronze; diffusion bonding; Ni interlayer; intermetallic compound

Microstructure analysis on composite coating of Fe-based alloy added WC by plasma cladding LU Jinbin, ZHANG Zhaojun, NING Jiuchao, LIU Hongtao (Department of Material and Chemical Engineering, Zhongyuan University of Technology, Zhengzhou 450007, China). p 65—68

Abstract: By plasma cladding and appropriate processing parameters, a coating metallurgically bonded to substrate was prepared on substrate of Q235 steel using Fe-based alloy adding 50% WC. The microstructure of the clad layer was investigated by SEM, XRD, EDS, and the microhardness distribution of the coating was also tested by microhardness tester. The results show that the WC particles in the composites are partly melted into the coating, and others distribute at the central and the bottom of the coating, which bond with the coating well. The coating with good bonding with substrate mainly consists of γ-Fe, WC, Fe_3W_3C, Fe_6W_6C and W_2C. The microhardness of the coating reaches 900～1 100 HV0.2.

Key words: plasma cladding; microstructure; microhardness; WC

Cavitation erosion resistance of plasma clad high chromium iron based coating by precursor carbonization-composition process LIU Junbo, YU Jiayang, WANG Limei, HAN Fang (School of Mechanical and Electronic Engineering, Weifang University, Weifang 261061, Shandong, China). p 69—72

Abstract: The high chromium iron based alloy coating was fabricated on the surface of medium carbon steel by plasma cladding using the powders by precursor carbonization-composition process. Microstructure, hardness distribution and cavitation erosion resistance were observed and measured by OM, X-ray diffraction, SEM, microhardness tester and ultrasonic oscillation magnetostriction strain gauge. The process of cavitation erosion was analyzed. The results show that the coating has high microhardness and good cavitation erosion resistance. The cumulative mass loss is only 49.8% as the one of 0Cr13Ni6Mo steel after 44 hours cavitation erosion. The excellent cavitation erosion resistance of the coaring is due to the following factors: the grain boundary of hard phase hinders plastic deformation of phase γ and the stress induces the phase γ changing to martensite structure.

Key words: plasma cladding; high chromium iron based coating; microstructure; cavitation erosion

Analysis on soldered joint reliability of PBGA package with different arrangement models DAI Wei, XUE Songbai, ZHANG Liang, SHENG Zhong (College of Materials Science and Technology, Nanjing University of Aeronautics and Astronautics, Nanjing 210016, China). p 73—76

Abstract: Finite element analysis was used to investigate the stress distribution of PBGA soldered joints with different arrangement models, and the constitutive relationship of Sn3.0Ag0.5Cu lead-free solder was described by Anand model. The results indicate that the positions of critical soldered joints are determined by the chip cor-